Int. J. Heat Mass Transfer. Vol. 36, No. 11, pp. 2725–2746, 1993
Printed in Great Britain

0017–9310/93 $6.00 + 0.00
Pergamon Press Ltd

Advances in transport phenomena during convective drying with superheated steam and moist air

P. PERRE,† M. MOSER‡ and M. MARTIN‡

†ENGREF, 14 rue Girardet, 54042 Nancy, France
‡LEMTA (URA CNRS n° 875), 2 av. de la Forêt de Haye, 54516 Vandoeuvre, France

(*Received* 5 *May* 1992 *and in final form* 4 *January* 1993)

Abstract—The latest developments in high temperature convective drying are presented. The process has been investigated experimentally and theoretically for two drying fluids: moist air and superheated steam, and for two materials: light concrete and softwood. The experimental investigation was made in an aerodynamic return flow wind-tunnel, using a new type of sensor which enables measurement of both temperature and pressure at the same point. The numerical model of heat and mass transfer developed over several years has been used to simulate the experimental test, in 1-D for concrete and in 2-D for softwood. Good agreement is obtained between the calculations and experiments. An analytical model taking into account the transfer mechanisms between the exchange surface and an assumed drying-front has also been developed, and enables the explanation of most of the phenomena observed, both in the experiments and the simulation. The main purpose of the present work was not only to determine the differences on the pressure and temperature fields, but also to give a physical explanation for the moisture migration at temperatures when the wet bulb is other than the boiling point. Finally, it is shown that the process can be divided into three domains: (a) an initial drying period, where the medium is at the wet bulb temperature; (b) a second phase with a stage more or less pronounced, at a temperature which depends on the air flow and on the material; and (c) a final stage, during which all the temperatures approach the dry bulb temperature.

1. INTRODUCTION

DRYERS are used to remove water from porous solid materials by evaporation. They are designed in many different ways in order to fulfil various requirements, such as high or low temperature drying at normal pressure, or under vacuum, with air or superheated steam as drying fluid. The heat necessary to evaporate the moisture may be supplied by conduction, by radiation, by convection through the drying fluid or by microwaves.

In practice, several different techniques are used: natural drying, vacuum drying (either continuous, by contact conduction, or discontinuous, by periodic convection), conventional convective drying at low temperature, dehumidification or heat pump drying systems, high temperature convective drying and more recently, microwave drying.

The selection of drying conditions is usually a compromise, resulting from the requirement to optimize product quality, while at the same time minimizing the size of the drying equipment or reducing the drying time.

The use of fast convective drying at high temperature, which has been investigated experimentally and theoretically for ten years in the authors' laboratory, requires a detailed analysis of moisture migration within the porous material to understand the mechanisms involved, and particularly the influence of the geometry or structure of the porous medium and the aerothermal conditions (velocity, dry and wet bulb temperatures).

To widen the scope of the investigation, two materials were tested: a slab of light concrete, and a softwood board, together with two drying fluids: moist air and superheated steam. The main interest of these two fluids is to be able to differentiate, or not, the wet bulb temperature and the boiling temperature, fixed at 100°C.

2. EXPERIMENTAL STUDY

2.1. *General description of the wind tunnel*

An aerodynamic wind tunnel (Fig. 1) was built in 1979 when work was first begun on high temperature convective drying [1, 2]. Since then, many improvements have been made.

The present configuration is shown of:

- a radial fan generating an adjustable fluid velocity in the range $2 < U < 15$ m s^{-1}, controlled by an anemometer located in the test section;
- a long insulated cylindrical return tube of 250 mm diameter, equipped with a diaphragm for measuring the mass flow rate;
- a preheating chamber, containing the electric heating unit, composed of four 22 kW resistances. A resistance thermometer, together with a PID controller connected to the heating element supply, ensure

NOMENCLATURE

C	molar concentration [mol m^{-3}]
C_p	specific heat [J kg^{-1} K^{-1}]
D	diffusivity [m^2 s^{-1}]
h	specific enthalpy [J kg^{-1}] or heat transfer coefficient [W m^{-2} K^{-1}]
Δh_v	latent heat of evaporation [J kg^{-1}]
K	intrinsic permeability [m^2]
k	relative permeabilities or mass transfer coefficient [m s^{-1}]
M	molar mass [kg mol^{-1}]
P	pressure [Pa]
q	drying rate [kg m^{-2} s^{-1}]
$\langle \dot{m} \rangle$	evaporation rate [kg m^{-3} s^{-1}]
R	universal gas constant [J mol^{-1} K^{-1}]
S	surface [m^2]
T	temperature [°C or K]
t	time [s]
U	velocity [m s^{-1}]
X	moisture content [kg of water/kg of solid]
x	molar fraction
z	distance [m].

Greek symbols

ε	volumic fraction
λ	thermal conductivity [W m^{-1} K^{-1}]
μ	dynamic viscosity [kg m^{-1} s^{-1}]
ν	kinematic viscosity [m^2 s^{-1}]
Π	porosity
ρ	density [kg m^{-3}]
ρ_0	apparent density [kg m^{-3}]
σ	surface tension [N m^{-1}]
ω	mass fraction.

Subscripts

a	air
atm	atmospheric
b	bound water
c	capillary or cellulose
cr	critical
eff	effective
eq	equilibrium
f	front
g	gas
ini	initial
irr	irreducible
l	liquid
fsp	fibre saturation point
s	solid
sat	saturated
v	vapour
vs	saturated vapour
∞	ambient.

Superscripts

g	intrinsic average over the gaseous phase
l	intrinsic average over the liquid phase
$-$	average value
$\approx$	order 2 tensor.

that the dry air temperature is accurate to one degree Celsius in the range 40–200°C:

- an aerodynamic convergent, just before the test section;
- a test section where the slab or the board is situated;
- an expansion tube, to counteract the rotational flow at the fan intake;
- an external boiler generating the low pressure steam injected into the preheating chamber.

Regulation of the moisture content of the air is based on measurement of the wet bulb temperature. An increase in the wet bulb temperature is obtained by increasing the boiler power and a decrease is produced by condensing the moist air at the surface of a water-cooled coil. The accuracy depends on the difference between the wet bulb and the dry bulb temperatures. It is of the order of one degree for small differences and can reach five degrees in extreme cases.

2.2. *Test section*

The test section dimensions are: $0.25 \times 0.25 \times 1.20$ m.

The samples (either slabs of light concrete or softwood boards) are placed in the horizontal plane of symmetry of the test section.

Since analysis of drying requires an accurate measurement of the water lost during the process, the weight is measured by using three rods attached to the sample and passing through the bottom of the test section, where they are supported by an electronic balance.

The different data concerning the slab or board (pressure, temperatures, weight, etc.) and the fluid flow (wet and dry bulb temperatures, velocity, etc.) are recorded through an acquisition power station connected to a computer.

2.3. *Instrumentation of the slab (or board)*

The main advantage of high temperature convective drying is to reduce the drying time. The acceleration of internal moisture transfer within the material is due to the development of an overpressure in the gaseous phase inside the slab (or board). This phenomenon explains why the temperature and pressure measurements are so important, requiring a careful choice of measurement techniques. In particular, since the overpressure can exceed one bar, a large error in tem-

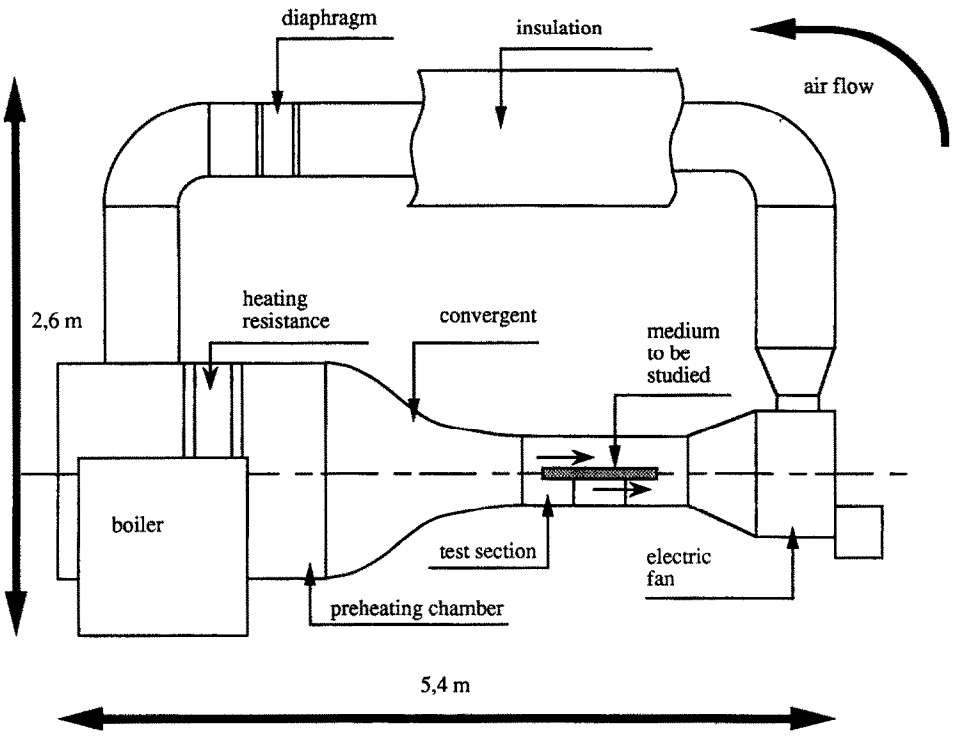

FIG. 1. Wind tunnel.

perature or pressure can result from a leak. To avoid this phenomenon, a new method was adopted. In addition, it allows temperature and pressure measurements simultaneously and at the same point [3].

Figure 2 shows the location of the chosen measurement points and the numerical 2-D domain. The surface temperatures $T0$ and $T6$ are available only in the simulation tests. The water and gas-tight measurement device is illustrated in Fig. 3.

For both materials, a hole was made at each measurement location. In the case of wood, the hole was smaller than the diameter of the sensor, so that the latter was forced into the board with the aid of a hammer. For concrete, only temperature measure-

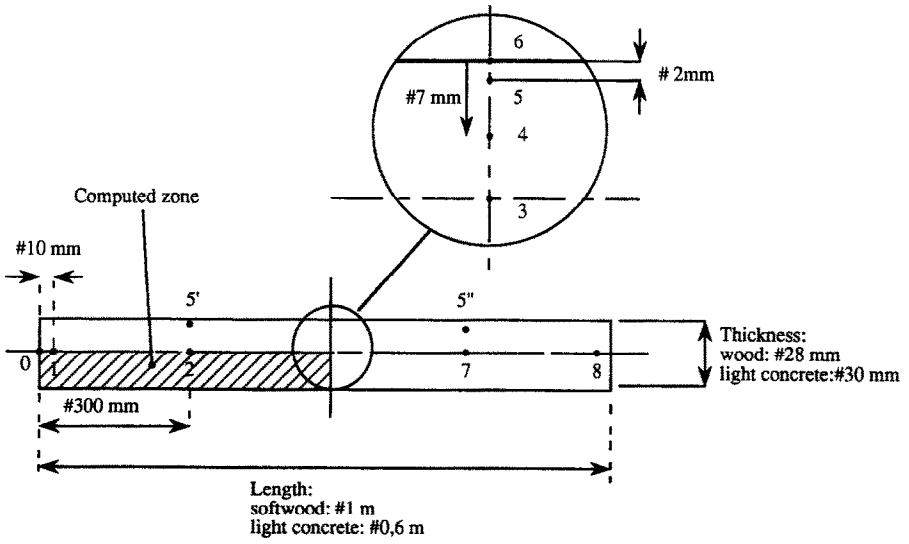

FIG. 2. Location of the measurement points and numerical 2-D domain.

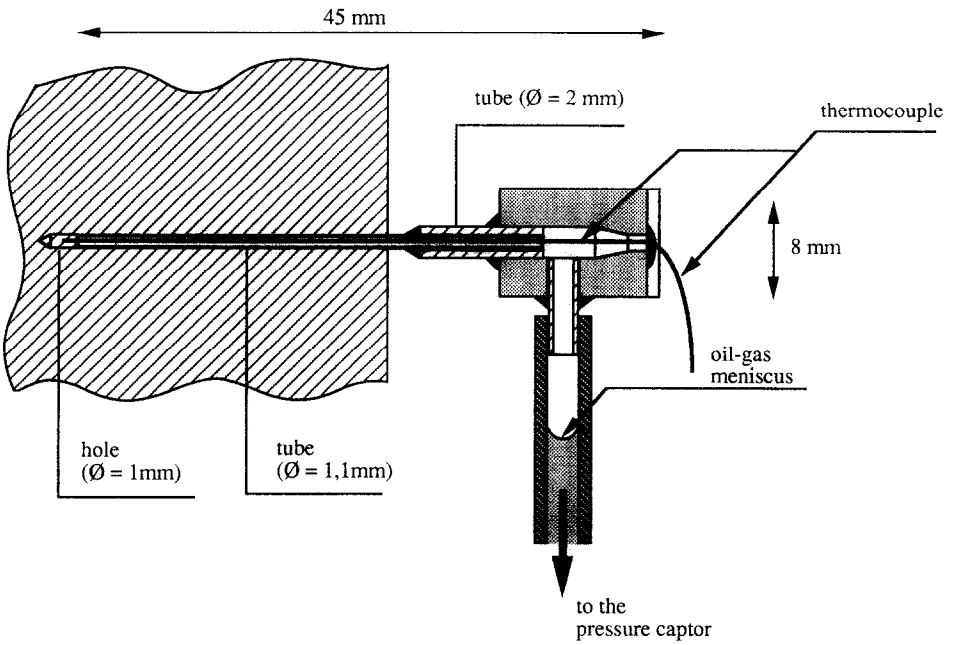

FIG. 3. Combined temperature and pressure sensor.

ments were carried out. The 3 mm wide hole was filled with silicon glue. Then, after the glue had been dried, the medium was saturated and the thermocouples were inserted in the glue.

Note that the technique adopted for concrete is a standard procedure [4, 5], which cannot be applied in the case of wood, since the latter is never dry before the test. A completely new type of sensor was developed for wood.

In order to avoid severe temperature and humidity conditions, the pressure captor is placed outside of the test section. The temperature difference between the measurement device and the pressure captor thus induces a convective movement of the stream, which condenses into the pressure captor. To prevent local evaporation, the pressure captor and the connecting tube were filled with oil, taking care to ensure an oil–gas interface inside the test section (that means over the boiling point).

2.4. *Light concrete*

The material used is a building material which has the advantage of being homogeneous, isotropic and reproducible. It has also a high permeability, of the order of 10^{-13} m^2 and a low hygroscopic range ($X_{hygro} = 0.07$). The dimensions of the slab are: $0.030 \times 0.15 \times 0.625$ m. Before each test the slab is saturated with water by several vacuum cycles.

2.5. *Softwood*

This material was chosen in order to study the influence of anisotropy, especially for the permeabilities, on the transfer mechanisms.

Wood is a living material which has a typical and very complex structure, depending on the species. Softwood was chosen for its well defined structure, which is simpler than that for hardwood.

The mechanism of sap rise is due to capillary forces in the liquid phase. The liquid flows from one tracheid to another through the bordered pits, comprising a membrane ('torus') which can move under the effect of the pressure and which can obstruct the passage of the fluid, thus preventing a break in the liquid column. This architecture is vital for the life of the trees and plays an important role during the drying process.

It is a hygroscopic material; the moisture content for which the cell walls are saturated, with no free water in the cell cavities, is called the fibre saturation point. This point is 30% of the ovendry weight, emphasising the large amount of water which can be absorbed.

Three directions of anisotropy are taken into consideration: longitudinal, radial and tangential. For softwood, the ratio of longitudinal to radial permeability is approximately in the range 100–10 000.

Heterogeneity is evident at all scales of observation. It is easy to distinguish earlywood from latewood, but the difference which exists between sapwood and duramen is very important too: in sapwood the moisture content can be twice as great and the permeability 100 times greater!

All these points emphasise the need to take great care in sampling. It was decided to experiment from a forest which belongs to the forest school of Nancy (ENGREF) to select a tree, and to chop it down just before the test. The cut-up plan was designed so that the board was taken from within the sapwood, ensuring good homogeneity and a high moisture content (up 200%).

3. EXPERIMENTAL RESULTS

3.1. *Light concrete experiments*

Among the 20 tests performed, the results of the three most representative ones are discussed here.

- The first test involved a superheated steam flow in the following conditions: velocity $U = 6\ \text{m s}^{-1}$ and dry bulb temperature $T_{dry} = 140°C$.
- The second and third tests used a moist air flow $U = 6\ \text{m s}^{-1}$, with two different temperature gaps $\Delta T_{dw} = T_{dry} - T_{wet}$ where: T_{dry} is the dry bulb temperature and T_{wet} is the wet bulb temperature. In the following text, the conditions of test 2 ($\Delta T_{dw} = 30°C$) will be denoted as 'soft' and those of test 3 ($\Delta T_{dw} = 90°C$) as 'hard'.

The aim of these two tests was to analyse the interactions between the internal and external moisture transfers.

Superheated steam (*Test* 1): $T_{dry} = 140°C$. Figure 4 shows the variation with time of the average moisture content and of the different temperatures within the slab.

It can be seen that the main effect of high temperature convective drying is a significant reduction in the drying time. In effect, when $T_{dry} = 140°C$ and $U = 6\ \text{m s}^{-1}$ seven hours are sufficient to reduce the moisture content of a slab of light concrete from 90% to about 2%.

The temperature versus time curves show a long plateau region at the boiling temperature ($T_{boiling} = 100°C$), followed by an increase up to the temperature of the steam flow. The deeper the location of the thermocouple, the greater is the duration of the plateau.

With superheated steam, the transition between the first drying period (evaporation from the exchange surface) and the second drying period (internal evaporation) has no discernible effect on the internal temperatures. In effect, the wet bulb temperature is equal to the boiling temperature, which remains constant at 100°C as long as the pressure remains equal to the atmospheric one.

Moist air 'soft conditions' (*Test* 2): $\Delta T_{dw} = 30°C$. Figure 5 represents the variation with time of the wet bulb temperature, the temperatures within the slab at points 3, 4 and 5, and the average moisture content of the sample.

It can be seen that good control of T_{wet} enables 'noise-free' curves to be obtained.

In these 'soft' aerothermal conditions, the drying process is much longer (13 h instead of 7 h).

The form of the temperature curves indicates three different phases:

- during the first two hours, the temperature curves show a plateau region at the wet bulb temperature (85°C). The temperatures in the slab being uniform and equal to $T_{wet} = 85°C$, the behaviour of the porous medium shows the existence of a period of constant drying rate (first drying period), which continues as long as the capillary suction drives water from the centre of the slab to the interface, where it is evaporated;
- above T_{wet}, the curves present a second plateau or a horizontal inflexion in the range 85–90°C;
- finally the temperatures continue to increase and reach the final flow temperature without any pronounced plateau at the boiling temperature $T_{boiling}$.

Moist air 'hard conditions' (*Test* 3): $\Delta T_{dw} = 90°C$. It can be seen in Fig. 6 that, owing to the large difference $T_{dry} - T_{wet}$, the temperature regulation is not as accurate as in the previous test, number 2.

The essential point to notice is the very fast drying process, which lasts only five hours, with the temperature variations being the same as in test 2. The temperatures go through a slight plateau at $T_{wet} = 70°C$,

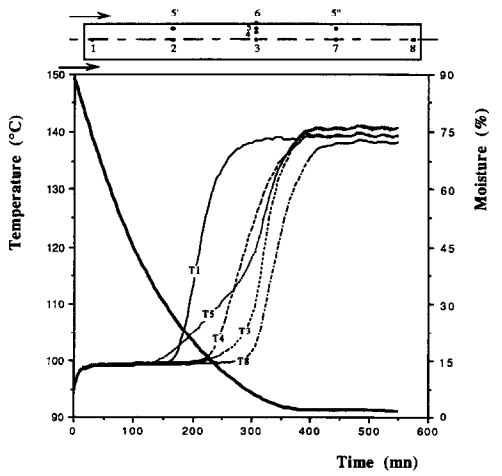

FIG. 4. Experimental drying of light concrete with superheated steam: Kinetic and temperatures (*T*1, *T*3, *T*4, *T*5, *T*8): $U = 6\ \text{m s}^{-1}$, $T_{dry} = 140°C$.

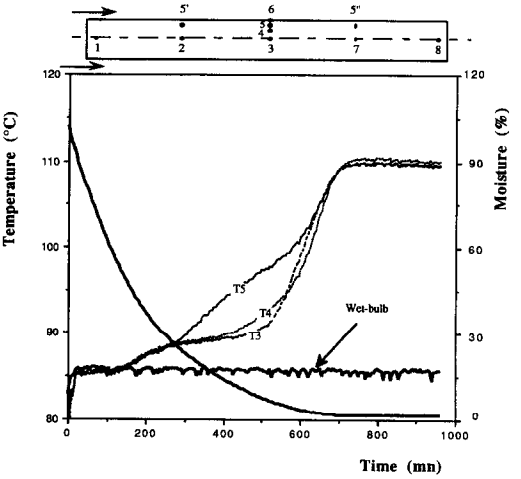

FIG. 5. Experimental drying of light concrete with moist air: Kinetic and temperatures (*T*3, *T*4, *T*5, wet-bulb): $T_{dry} = 115°C$, $T_{wet} = 85°C$.

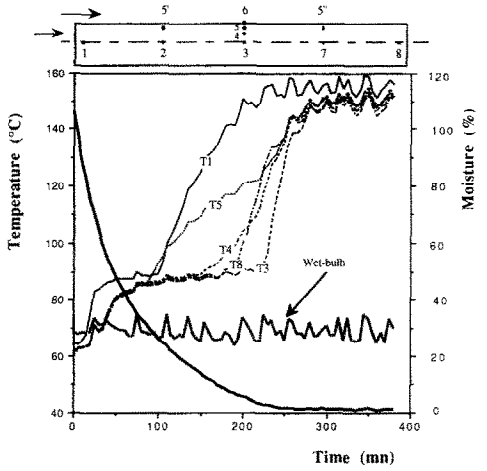

FIG. 6. Experimental drying of light concrete with moist air: Kinetic and temperatures ($T1$, $T3$, $T4$, $T5$, $T8$, wet-bulb): $T_{dry} = 160°C$, $T_{wet} = 70°C$.

then increase up to a second plateau in the range 85–90°C, beyond which they rise steeply through the boiling temperature until they attain the dry bulb temperature of the moist air flow.

3.2. *Softwood experiments*

Although about 20 tests were performed, because of the good reproducibility resulting from very careful sampling, only certain significant results are presented here.

Superheated steam (*Test* 4): $T_{dry} = 160°C$. Figure 7 shows on the same graph, the variation with time of the average moisture content of the board and the temperatures in the wood at points 1, 3, 4, 5 and 8.

While the drying times for a slab of light concrete and a board of softwood can be seen to be similar, the situation is quite different as regards the variation of temperature with time.

In effect, Fig. 7 reveals that not all of the temperatures in the board show a long plateau at the boiling temperature, contrary to the case for a slab of light concrete. Only a slight effect at about 100°C is observable during the first 50 min of drying.

The temperatures $T3$, $T4$ and $T5$ then cross the boiling point without levelling off, and continue to increase up to the temperature of the superheated steam flow. Note that $T3$ seems to remain close to 115°C for a short time before a quick rise towards the dry bulb temperature. Simultaneously, the temperatures measured by thermocouples $T1$ and $T8$, located at the front end and at the rear end of the board, present a long plateau at the boiling temperature. They then increase very rapidly (due to the close proximity of several exchange surfaces), overtaking $T3$, $T4$ and $T5$, and attain the temperature of the steam flow.

This phenomenon can be explained by the combination of the pressure which develops inside the board and the high longitudinal permeability of softwood (100 to 10000 times the transverse permeability).

To illustrate this remark, Fig. 8 shows the variation with time of the pressure and temperature measured at the same point in the board (2 and 7).

The correlation between the increase of temperature and the overpressure can be clearly seen. The two curves differ only at the end of the drying process when the board is in the hygroscopic range.

Figure 9 represents the variation with time of the moisture content of the board and of the pressure measured at different thicknesses (points 3, 4 and 5).

At the beginning of the process, the pressure increase can be seen to start close to the surface and to move progressively towards the centre of the board. Such a pressure variation indicates clearly that the surface of the board enters the hygroscopic range before the centre.

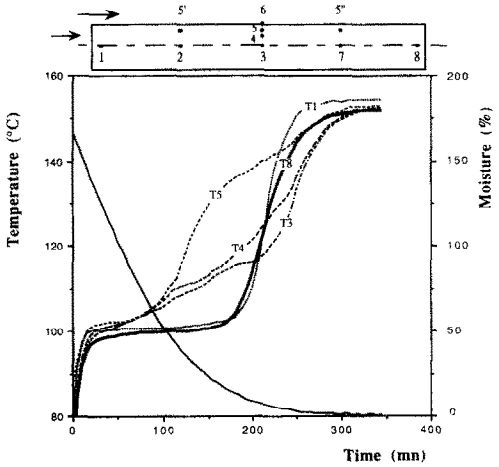

FIG. 7. Experimental drying of softwood with superheated steam: Kinetic and temperatures ($T1$, $T3$, $T4$, $T5$, $T8$): $U = 10\ m\ s^{-1}$, $T_{dry} = 160°C$.

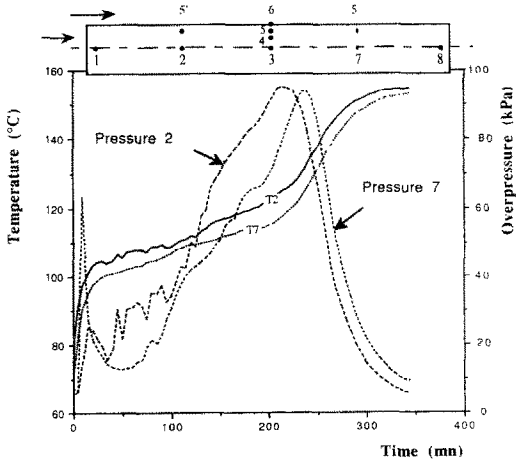

FIG. 8. Experimental drying of softwood with superheated steam: temperatures ($T2$, $T7$) and overpressures ($P2$, $P7$): $U = 10\ m\ s^{-1}$, $T_{dry} = 160°C$.

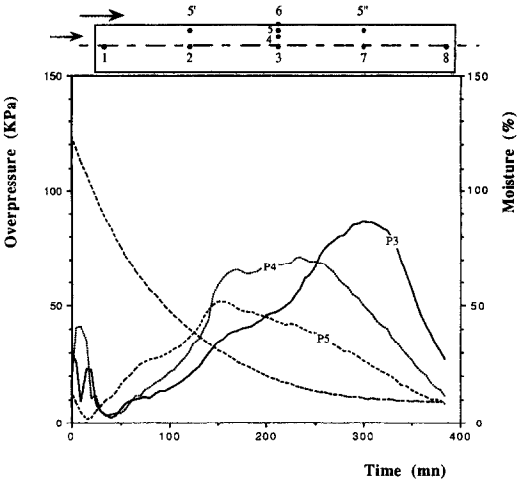

FIG. 9. Experimental drying of softwood with superheated steam: Kinetic and overpressures (*P3*, *P4*, *P5*): $U = 10\ \text{m s}^{-1}$, $T_{dry} = 160°C$.

In fact, the pressure follows the temperature variations in the thickness of the board.

The overpressure is strongly dependent on the values of the permeability, the drying rate and the distance between the evaporation front and the surface. It is maximum at the centre of the board.

Moist air 'soft conditions' (*Test* 5): $\Delta T_{dw} = 33°C$. Figure 10 gives the principal results. It can be seen that the choice of the following aerothermal conditions, $T_{dry} = 115°C$, $T_{wet} = 82°C$ and $U = 5\ \text{m s}^{-1}$, leads to a large increase in the drying time (20 h) and to a characteristic temperature variation.

The temperatures *T3*, *T4* and *T5*, measured respectively at the centre, mid-thickness and at the surface, show a plateau near $T_{wet} = 82°C$, followed by a rapid rise up to 105–110°C before reaching the dry bulb temperature. As was observed for light concrete, softwood presents an initial constant rate period. Nevertheless, no plateau is observed at the boiling temperature.

The variations of temperatures *T5′*, *T5* and *T5″* are identical. A slight shift occurs between the three temperatures, owing to the localization of the measurement points. The closer the measurement points are to the leading edge of the board, the faster the rise in temperature. The temperature *T1* increases slower than the previous ones till 12 h. Then it reaches very quickly the dry bulb temperature.

Moist air 'hard conditions' (*Test* 6): $\Delta T_{dw} = 58°C$. The variation with time of the moisture content and the temperatures are represented in Fig. 11.

The aerothermal conditions imposed on the material, namely $T_{dry} = 140°C$, $T_{wet} = 82°C$ and $U = 7\ \text{m s}^{-1}$, significantly modify the drying time (9 h) and also the temperature fields.

Indeed, no plateaus are observed, either at T_{wet} (no constant rate period) or at $T_{boiling}$. The temperatures increase progressively to reach the dry bulb temperature of the moist air flow.

3.3. *Discussion*

For light concrete, in the case of superheated steam drying, a long plateau at the boiling point is observable on the internal temperatures. Consequently, the observation of only the centre temperature suggests a mechanism involving too long a period of constant drying rate.

The two tests involving a moist air flow facilitate the interpretation, and clearly demonstrate:

- the existence of a constant drying rate period;
- the presence of a plateau in the temperature curves in the range 85–90°C.

Nevertheless, some differences can be seen:

- for low values of ΔT_{dw}, the temperature variations show a long constant rate period, followed by a plateau close to 90°C;
- for high values of ΔT_{dw} the drying process is faster

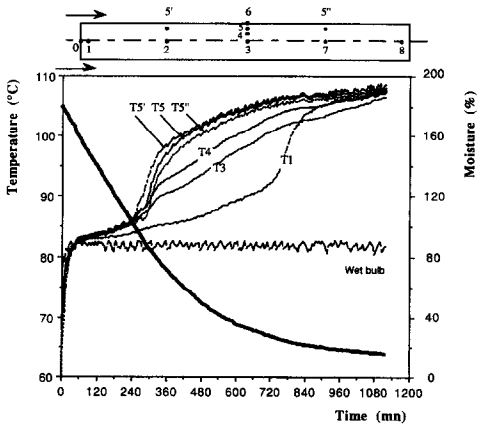

FIG. 10. Experimental drying of softwood with moist air: Kinetic and temperatures (*T1*, *T3*, *T4*, *T5*, *T5′*, *T5″* and wet bulb): $T_{dry} = 115°C$, $T_{wet} = 82°C$.

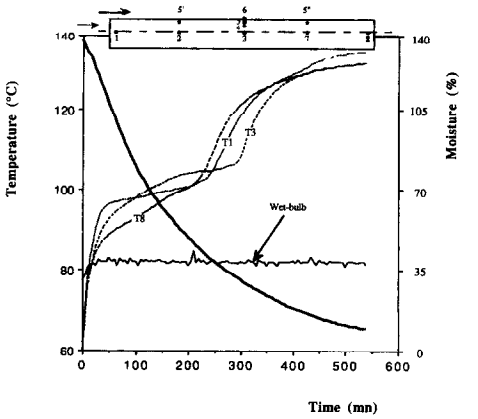

FIG. 11. Experimental drying of softwood with moist air: Kinetic and temperatures (*T1*, *T3*, *T8*, wet-bulb): $T_{dry} = 140°C$ and $T_{wet} = 82°C$.

and the constant rate period still exists, but the plateau at 85–90°C is more pronounced.

For softwood, there are generally fewer plateaus than for light concrete.

With a superheated steam flow, only the temperatures close to the leading and trailing edges of the board show a large plateau at $T_{boiling}$. This phenomenon is due to the high longitudinal permeability of softwood. In many papers, all the temperatures usually show a long stage at the boiling point [1, 2, 4–7].

With a moist air flow, a plateau at T_{wet} is observable when the drying conditions are 'soft'. Such a period at the wet bulb temperature never appears in the literature [4–7]. On the contrary, most authors report a long period at the boiling temperature.

In the present experiments, the period T_{wet} disappears for 'hard' conditions and the period at $T_{boiling}$ never appears.

4. DRYING SIMULATIONS

4.1. *The numerical code 'TRANSPORE'*

Over a number of years, a numerical code has been developed and improved in order to simulate heat and mass transfers in porous media [8–10]. The formulation, which is derived from the work of Whitaker [11], has been reviewed and adapted to cover all practically encountered configurations (non-uniform pressure for the gaseous phase, effect of pit aspiration on permeabilities, bound water migration, differential heat of sorption, etc...).

The code was first developed for softwood and for one dimension in space. It is presently available in 2-D geometries for softwoods, granular porous media and light concrete.

The elementary breakdown is based on the notion of control domain [12]. This numerical method, which respects the conservation balances with great accuracy, treats the gaseous phase both below and above the boiling point [13]. All intensive processes can be simulated (vacuum, contact, and microwaves drying, internal vaporization, etc...) while it is naturally adapted to high temperature convective drying [14].

In the following description, this code will be referred to as 'TRANSPORE' (Coupled TRANSfers in PORous mEdia).

It is not intended here to describe the model again: only the set of mathematical equations and the physical parameters are reproduced in the present paper (see Appendices 1 and 2). For more details concerning the code, the reader is invited to consult previous publications [8–10].

All the experiments presented in Section 3 have been simulated. The key point is a very close agreement between theory and experiment. Another important result is the ability of such an effective model to explain all the experimental observations.

4.2. *Light concrete*

Light concrete is an isotropic medium. Consequently, keeping the geometrical configuration in mind, it is sufficient to perform the calculations for unidirectional transfers. The three runs presented below have been computed with a regular grid comprising 81 nodes.

Superheated steam (*Run* 1): $T_{dry} = 140$°C. For this fluid, the wet bulb temperature equals the boiling point. The simulation shows that the long period at 100°C observed in the experiments is in fact divided into two parts (Fig. 12).

The first part is a real constant drying rate period, with liquid migration up to the surface, evaporation and vapour flux in the boundary layer. In the numerical code, the surface temperature ($T6$) is available: the departure of the latter from the wet bulb temperature, which in this case, equals the boiling point, marks the end of the constant drying rate period.

In the second part, a drying front appears in the medium. Evaporation occurs inside the medium. Nevertheless, the gaseous permeability is high enough to evacuate the vapour flux by a slight overpressure. The temperature which can produce this overpressure according to the saturated vapour curve is very close to 100°C. The temperature increases only in the dry zone, where a thermal gradient is required in order to transport the energy of vaporisation towards the front position.

The inward advance of the front inside the medium can be followed by the successive breakaways of the different internal temperatures ($T5$ and $T4$). When the centre temperature ($T3$) increases beyond 100°C, the first drying period has been finished for a long time. At this stage, the whole medium is in the hygroscopic range and the process is coming to an end. The drying rate decreases sharply and temperatures increase rapidly.

Moist air (*Runs* 2 *and* 3): $\Delta T_{dw} = 30$ C and $\Delta T_{dw} = 90$°C. Due to the separation between the wet

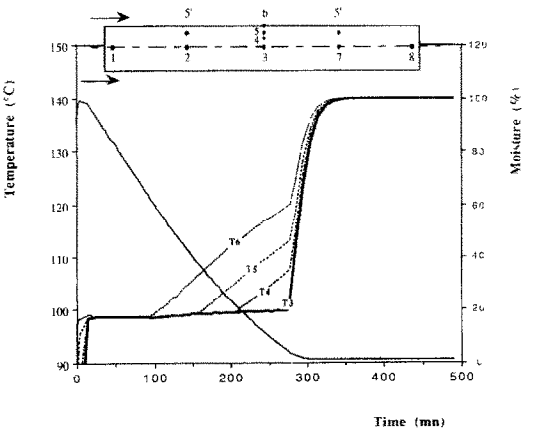

FIG. 12. Theoretical drying of light concrete with superheated steam: Kinetic and temperatures ($T3$, $T4$, $T5$, $T6$): $U = 6$ m s^{-1}, $T_{dry} = 140$°C.

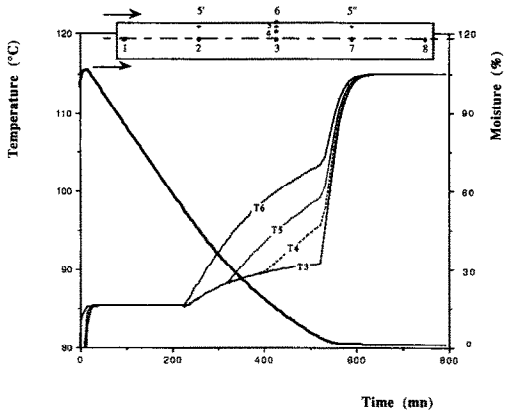

FIG. 13. Theoretical drying of light concrete with moist air: Kinetic and temperatures ($T3$, $T4$, $T5$, $T6$): $T_{dry} = 115°C$, $T_{wet} = 85°C$.

bulb temperature and the boiling point, the case of moist air is more interesting to analyse.

In both runs, the numerical curves show a first drying period for which all the temperatures remain close to the wet bulb temperature. However, this period is much shorter (≈ 20 min compared to 200) in the case of severe drying conditions (Figs. 13 and 14).

A period of decreasing drying rate then appears. From the successive departures of the temperatures from the value at the centre, it is obvious that a drying front moves within the medium. Up to this point, the process remains similar to the previous one (run 1).

What is new here is the variation of the centre temperature. At the end of the constant drying rate period, the value increases slowly from the wet bulb temperature up to about 90°C (i.e. 10°C below the boiling point!). It is to be noted that this evolution is the same for the two tests (low and severe drying conditions). This stage at about 90°C can be explained by an analytical model (see Section 5).

When the front reaches the centre of the slab, all the temperatures increase rapidly up to the dry bulb temperature. This final period resembles that observed in the test with saturated vapour.

In conclusion, for this medium, the numerical results can be seen to be in perfect accordance with all the experimental observations. Not only the shape of the curves but also the absolute values of the temperatures, average moisture content and the durations of each drying period are in excellent agreement with the experimental measurements.

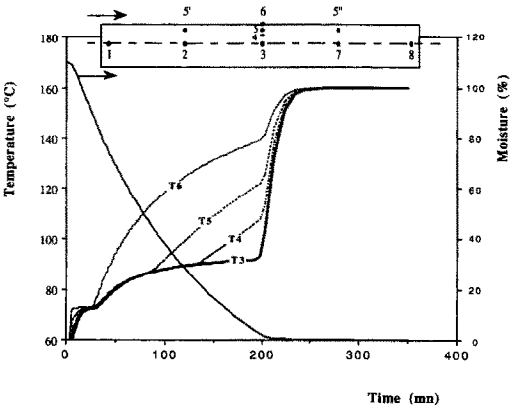

FIG. 14. Theoretical drying of light concrete with moist air: Kinetic and temperatures ($T3$, $T4$, $T5$, $T6$): $T_{dry} = 160°C$, $T_{wet} = 70°C$.

4.3. *Softwood*

Softwood is a strongly anisotropic medium. In cases where the internal pressure plays an important role, only 2-D simulations are able to reveal the true transfer mechanisms. The geometrical configuration used for softwoods is shown in Fig. 2. All the results have been computed with a 21×41 grid, uniform through the thickness ($\Delta x = 0.75$ mm) and non-uniform along the length ($\Delta y = 2$ mm close to the extremity and increases continuously up to 20 mm at the mid-point).

The three runs presented here (4–6) simulate respectively the tests 4–6. For each case, the order of magnitude of the heat transfer coefficient was determined from the maximum drying rate obtained during the experiment. Insufficient information was available to be able to take account of end effects and the development of a boundary layer: the code therefore assumes a constant exchange coefficient over all of the exchange surfaces.

Superheated steam (*Run* 4): $T_{dry} = 160°C$. Figure 15 shows the variation of the average moisture content (MC), temperatures and overpressures at different points. The shapes of these curves are identical to the experimental results (Figs. 7 and 8). The length of the constant drying rate period (all temperatures close to the wet bulb temperature) is about 80 min in both cases.

At the end of this period, the numerical temperatures increase more quickly than in the experiment. Moreover, in the case of the surface temperature ($T6$), which is available only for the simulations, the latter effect is even more marked.

The value of the transverse permeability (none of the parameters were adjusted) has an important effect during this drying period. Any slight underestimation of this parameter leads to a higher temperature, lower drying rate and longer total drying time (500 min against 300 min). Note that the description is not too bad: all the orders of magnitude agree with the experiment. In particular, it is to be noted that the 2-D version of the 'TRANSPORE' code is capable of predicting the end effects: in perfect agreement with the experiment, the end temperature ($T0$ and $T1$ are nearly the same for this run) shows a plateau close to the boiling point during the second drying period and then increases rapidly, overtaking all the mid-point temperatures, and is the first to reach the dry bulb temperature. At this point, the temperature $T3$ can be

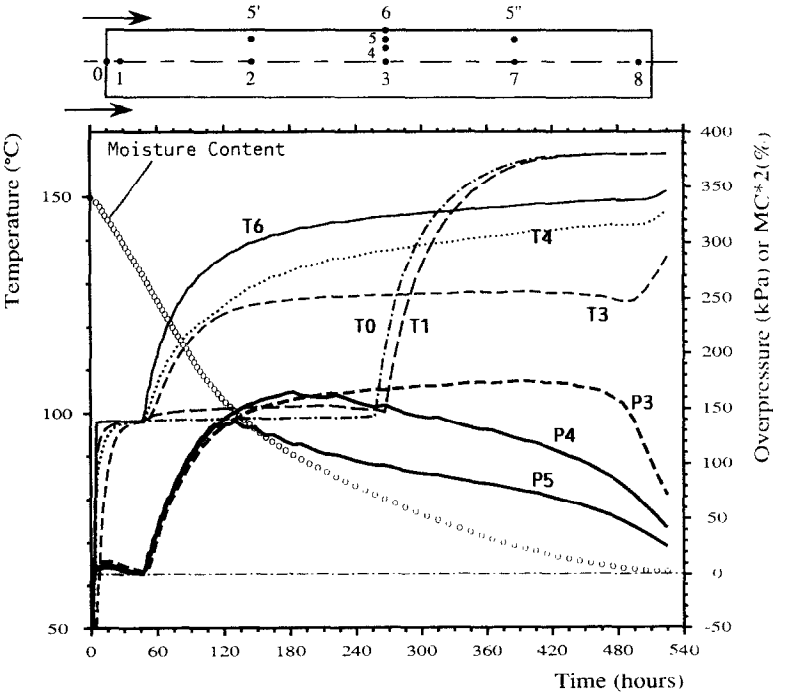

FIG. 15. Theoretical drying of softwood with superheated steam: Kinetic, temperatures and pressures. $U = 10$ m s^{-1}, $T_{dry} = 160$ C.

seen to decrease slightly, which is surprising during a drying process. In fact, the extremities have just become completely dry, leading to an increase in the relative longitudinal permeability to the gaseous phase, allowing a greater longitudinal vapour flux for the same overpressure. The latent heat required is momentary greater than the thermal flux and reduces the temperature.

It is interesting to compare the evolution of the temperature and the pressure at the same position (points 3 and 4): for the initial transient period, the temperature, and thus the pressure, increases. During the constant drying rate period, the temperature remains constant within the medium but the liquid extraction increases the volume of the gaseous phase and decreases the partial pressure of dry air. Consequently, it is quite normal to observe a slight decrease in the total pressure. At the beginning of the second drying period, temperature and pressure change in a closely similar manner. The temperature increases as long as the resulting overpressure is great enough to evacuate the vapour evaporated by the thermal flux.

This mechanism continues as long as the moisture content remains above the fibre saturation point (about 500 min for point 3 and 200 min for point 4). The temperature subsequently increases towards the dry bulb value, whereas the pressure decreases. Therefore the evolutions of *P3*, *P4*, *P5* point out the development of a dried zone from the exchange surface towards the centre.

All the phenomena described here can be seen in the experimental results (Fig. 8). Pressures measured at different thicknesses indicate the corresponding start of the hygroscopic domain. Once again, these curves show good agreement with the experimental observations (Fig. 9).

A more severe test is to represent the locus of a given point in the board in the graph of pressure vs temperature. It is of great interest to notice that the experimental curve (Fig. 16(a)) is tangential to the saturated vapour pressure curve.

Because of the partial pressure of dry air, which is never equal to zero, the computed pressure (Fig. 16(b)) is always greater than the saturated vapour pressure, for the part of the curve concerning the free water domain. Comparison with the experimental results suggests that the sensors are not perfectly airtight. Note that the air cannot be renewed inside the wood: a very slight gas leak is sufficient to nullify the partial pressure of dry air.

Moist air 'soft conditions' (*Run* 5): $\Delta T_{dw} = 33$ C. In this case, the experiment indicated a real first drying period, with a board temperature very close to the wet bulb temperature. This period can also be seen on the computed curves (Fig. 17). Moreover, its duration agrees with that observed experimentally (about 200 min).

At the end of this constant drying rate period, all the mid-length temperatures increase together rapidly. This point does not agree with the experiment. Once again, the relative permeability to the gaseous phase seems to be too low. The dried zone moves very slowly

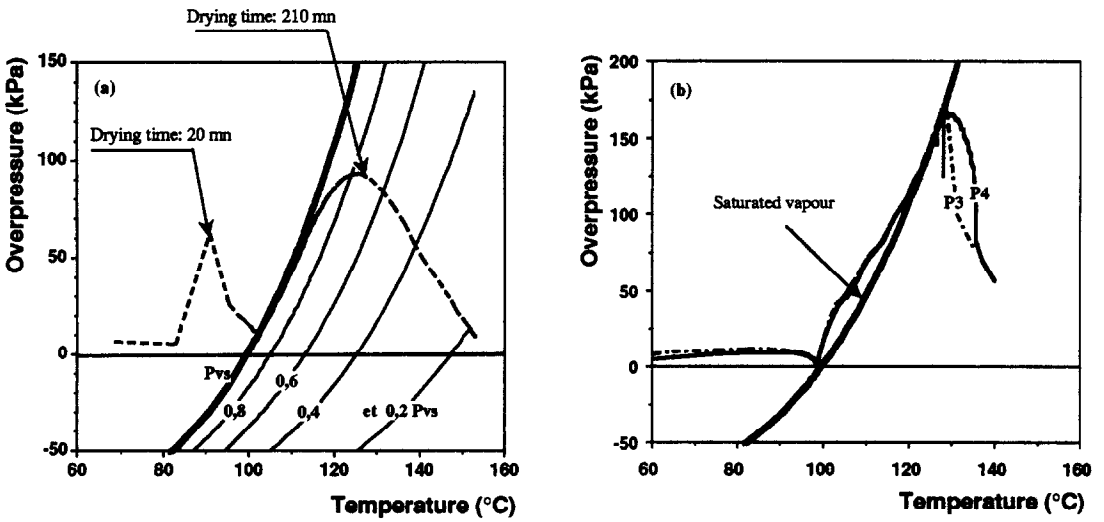

FIG. 16. Experimental (a) and theoretical (b) overpressures representation in the pressure–temperature plane.

towards the centre. About 750 min are required before the temperature near the surface ($T5$) pulls away from the other temperatures. This difference is confirmed by the slow variation of the global moisture content.

It is clear from both calculation and experiment that no specific behaviour is observed on passing through the boiling point.

We can notice for this case that the evolutions of temperatures $T0$ and $T1$ are quite different. At the end of the constant drying period the temperature $T0$ remains at the wet bulb temperature for 500 min whereas $T1$ increases slowly during the same time. The last one shows an evolution similar to the corresponding experimental point (Fig. 10).

Moist air 'hard conditions' (*Run* 6): $\Delta T_{dw} = 58°C$. In this case, the board experiences very severe drying conditions (large difference between the dry and wet bulb temperatures and high air velocity). The stage at the wet bulb temperature is just perceptible (Fig. 18). In accordance with the experiment, and although the

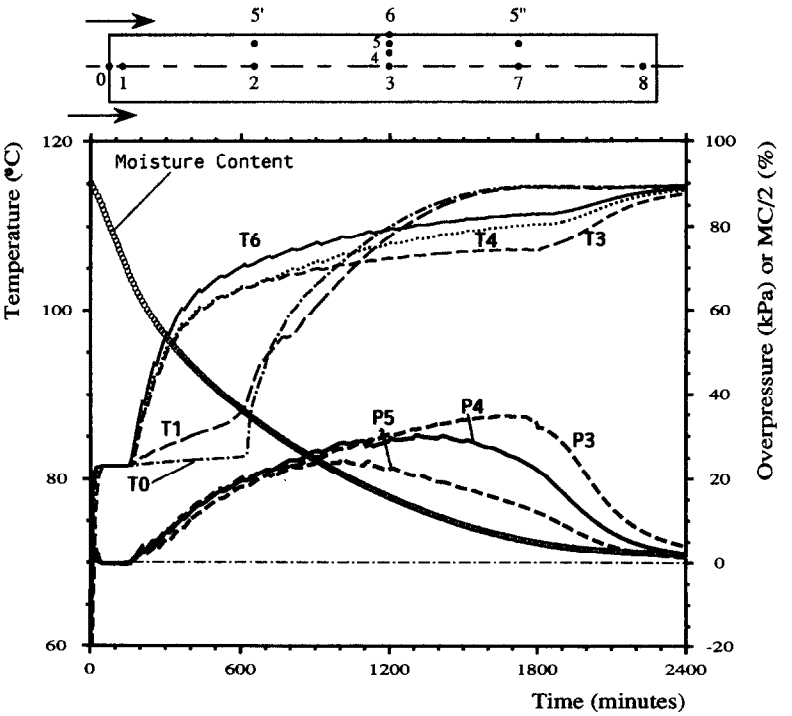

FIG. 17. Theoretical drying of softwood with moist air: Kinetic, temperatures and pressures. $T_{dry} = 115°C$, $T_{wet} = 82°C$.

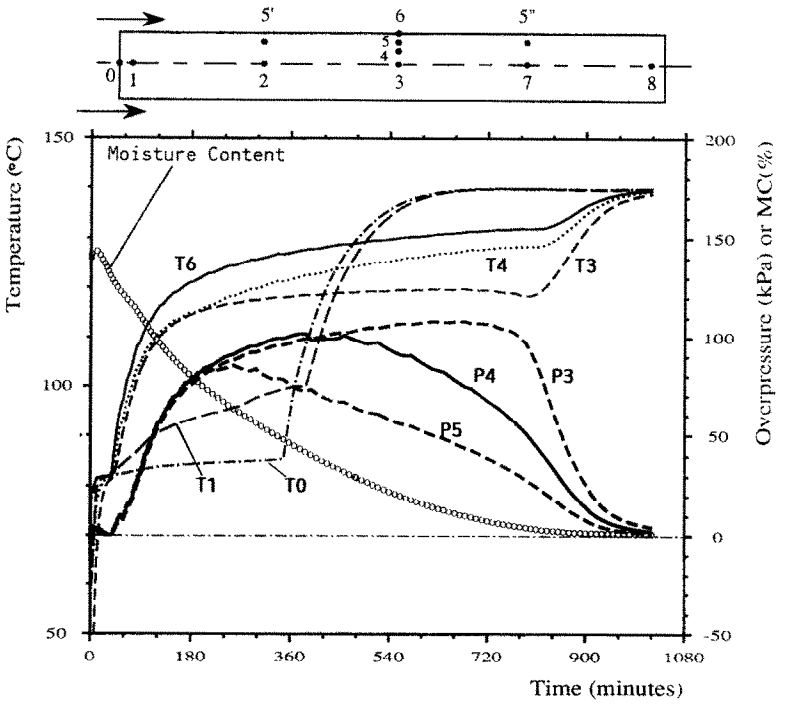

FIG. 18. Theoretical drying of softwood with moist air: Kinetic, temperatures and pressures. $T_{dry} = 140$ °C, $T_{wet} = 82$ °C.

initial moisture content was high, the first drying period disappears.

Only the end temperature ($T1$) remains stationary at the boiling point. The others increase directly up to about 110–120 C, the value required in order to ensure the drying rate corresponding to the heat supplied.

Before reaching the hygroscopic domain, the centre temperature ($T3$) decreases slightly: this phenomenon has been explained in the comments on run 4.

The many analogies with superheated steam drying (run 4) should be noted. The greater difference during the first drying period must be attributed to the overpressure effect. Indeed, with superheated steam, the temperature within the board attains the boiling point during the first drying period: large overpressure acts on the liquid from the start of the drying. With moist air drying, as long as the surface is above the fibre saturation point, the board tends towards the wet bulb temperature, i.e. below the boiling point. During this period, no significant overpressure is observed: the process resembles low temperature drying [9] and only the capillary action is able to drive the liquid towards the surface.

4.4. *Bi-dimensional plots*

The numerical code is able to provide much more information than simply the variation in temperature, moisture and pressure at certain chosen points of the board. 3-D surfaces are presented here to illustrate how the coupled transfers occur at high temperature and in a 2-D geometry. The numerical domain is represented on Fig. 2, the visible faces (the axis) are the exchange surfaces and the hidden ones are the planes of symmetry. The model has now become a real tool which can be used to understand the process.

The three runs analysed here are the first involving saturated vapour (run 4: elapsed times: 1, 2, 5, 6 h) and the two following ones with low and high severity drying in moist air (run 5 and run 6). The different variable fields illustrated by temperature–moisture content–pressure surfaces for different drying times must be connected together in order to reconstruct the process (effect of temperature on pressure, effect of pressure on gas and liquid transport, effect of moisture content on partial vapour pressure, etc.). While all the comments made in the previous sections remain valid, some particular effects are illustrated by these 3-D surfaces.

Figures 19–21 concerning run 4, are given as an example of the evolutions on the main parameters.

We note:

- the overpressure throughout the process;
- the effect of this overpressure on the mass transport in the longitudinal direction;
- the difficulty of transport in the hygroscopic range;
- the stationary end temperature at the boiling point;
- the effect of longitudinal gaseous diffusion, at the end of the process, even far from the extremity of the

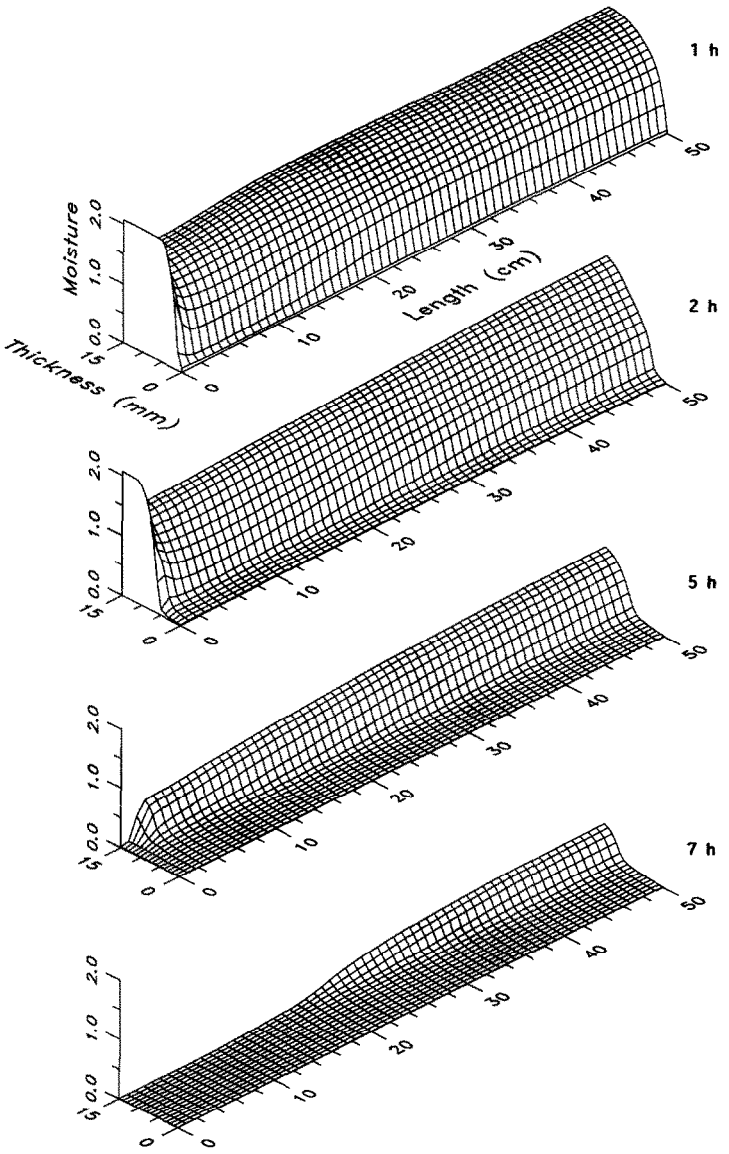

FIG. 19. Theoretical drying of softwood with superheated steam: moisture at different drying times (1, 2, 5, 7 h).

board. This effect must be connected with the decrease of $T3$.

For 'soft conditions' in moist air (run 5, $\Delta T_{dw} = 33°C$) we would be able to observe on the corresponding figures:

- the initial drying period at the wet bulb temperature;
- the low pressure during this period;
- the increase of pressure and, in consequence, the longitudinal liquid transport when the medium passes through the boiling point (at 7 h). This transport feeds the end of the board which remains above the fsp and close to the wet bulb temperature;
- the attainment of the dry bulb temperature on all exchange surfaces when the extremity finally reaches the hygroscopic range. At this point, the liquid remaining in the centre of the board disappears by both transverse and longitudinal transfers;
- the similarity of the process to the previous run after the end of the initial drying period.

For 'hard conditions' in moist air (run 6, $\Delta T_{dw} = 58°C$) we notice that the first drying period disappears. Consequently the effects are similar to the ones observed in run 4.

5. ANALYTIC MODEL

5.1. *Presentation of the model*

The aim of this section is to explain the existence of a temperature plateau close to 86°C observed dur-

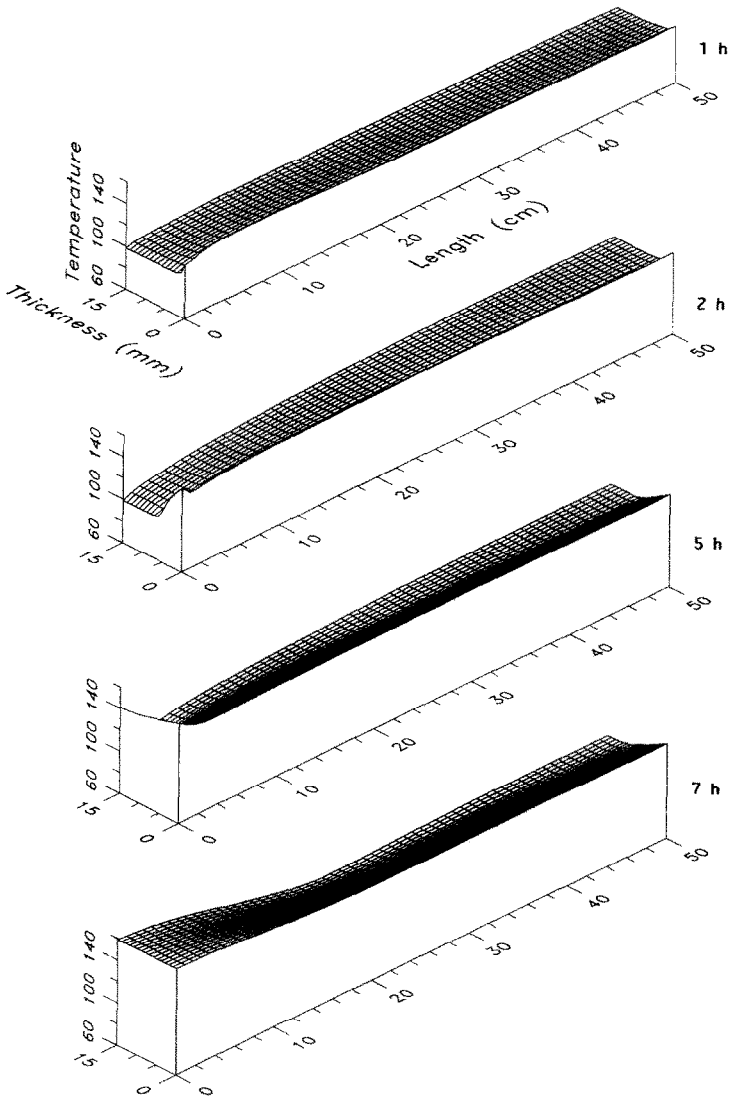

FIG. 20. Theoretical drying of softwood with superheated steam: temperatures at different drying times (1, 2, 5, 7 h).

ing moist air drying of light concrete, using a one-dimensional analysis incorporating certain simplifying assumptions.

The analytical model developed makes it possible to study low or high temperature drying as well as the transition between the convective and diffusive transfer modes.

During the convective drying of a slab of light concrete, a drying front propagates from the surface to the centre; the porous medium being divided into two zones: a liquid zone and a vapour zone, where transport occurs only in the gaseous phase (Fig. 22).

In the vapour zone, where $\bar{u}_l$ and $\bar{u}_b$ are equal to zero, an arrangement of equations (A4)–(A7) leads to:

$$\rho_0 \frac{\partial X}{\partial t} + \nabla \cdot (q_v) = 0 \qquad (1)$$

$$\frac{\partial \rho_a}{\partial t} + \nabla \cdot (q_a) = 0 \qquad (2)$$

in which the mass fluxes of vapour q_v and air q_a are given by:

$$q_v = \bar{\rho}_v^g \bar{u}_v \quad \text{and} \quad q_a = \bar{\rho}_a^g \bar{u}_a.$$

If the problem is considered to be quasi stationary (without accumulating terms) the mass fluxes q_a and q_v are constant in the vapour zone:

$$q_a = \text{const.} \quad \text{and} \quad q_v = \text{const.}$$

With a liquid–gas interface, the non-miscibility of air in the liquid implies $q_a = 0$. However, inside a porous material, this hypothesis is not so obvious, since it is necessary to consider what happens throughout the thickness of the liquid phase. If, firstly, the phenomenon is quasi-stationary and, secondly, the

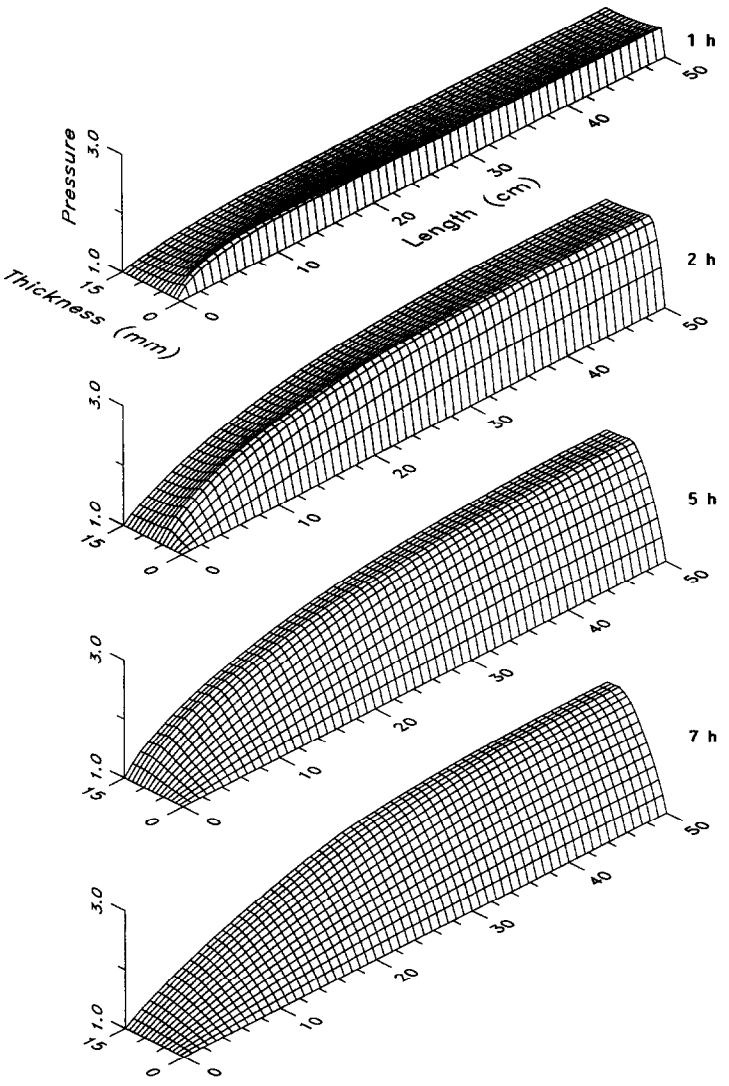

FIG. 21. Theoretical drying of softwood with superheated steam: pressure at different drying times (1, 2, 5, 7 h).

temperatures and pressures are uniform, the mass flux of air is still equal to zero at the front position (see equations (A8), (A12) and (A15)).

The general expression of the mass flux of vapour:

$$q_v = \omega_v(q_a + q_v) - \rho_g D_{eff} \nabla \omega_v \tag{3}$$

can be simplified and written as:

$$q_v = \frac{-\rho_g D_{eff} \nabla \omega_v}{1-\omega_v} \tag{4}$$

in which D_{eff} is the effective diffusivity and ω_v the mass fraction of vapour.

By using the perfect gas law, and developing the gradient of mass fraction of vapour, we can then write:

$$\nabla \omega_v = \frac{M_a \cdot M_v}{(P_a \cdot M_a + P_v \cdot M_v)^2}(P_g \nabla P_v - P_v \nabla P_g). \tag{5}$$

A convective term generated from the total pressure gradient induced by diffusion is therefore observed.

In order to analyse this complex mechanism, it is necessary to study the variation of the pressure of the vapour within the slab and to examine the influence of permeability.

The mass flux of vapour q_v can be expressed by using a development of ω_v and $\nabla \omega_v$ and introducing the Darcy law, in which K_g and ν_g are the intrinsic permeability and the gaseous viscosity:

$$q_v = -\frac{K_g}{\nu_g} \nabla P_g. \tag{6}$$

By substituting new parameters:

$$K^* = \frac{K_g}{\nu_g} \quad \text{and} \quad D^* = \frac{D_{eff} M_v}{RT} \tag{7}$$

q_v can be written as follows:

$$q_v = -\frac{D^* \nabla P_v}{1 + \frac{P_v}{P_g}\left(\frac{D^*}{K^*} - 1\right)}. \tag{8}$$

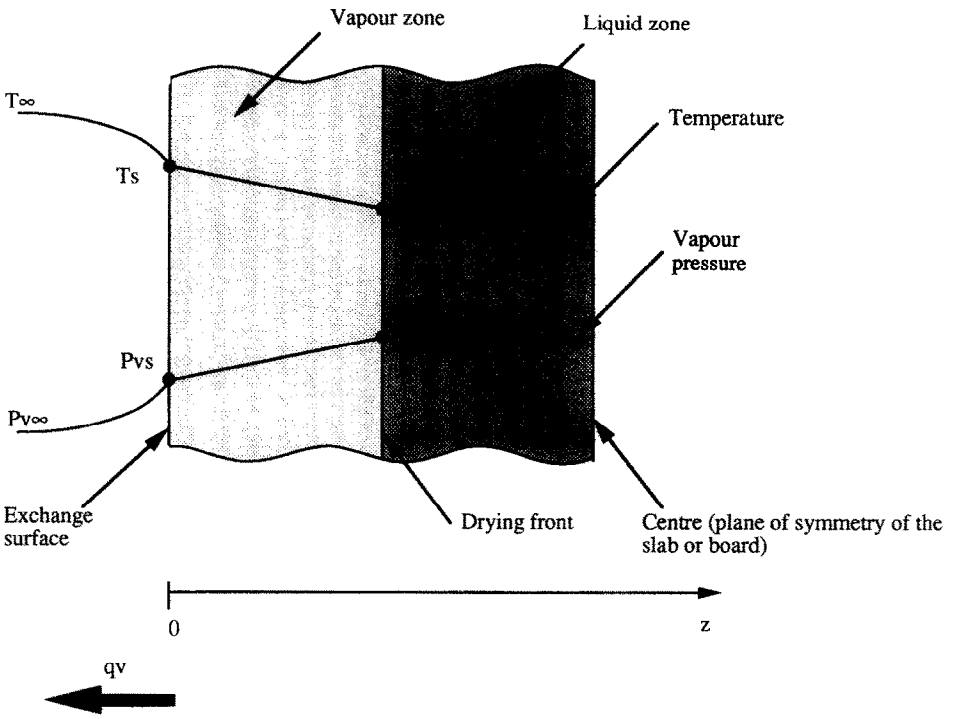

FIG. 22. Schematization of the drying front hypothesis.

A short discussion of the effect of the total pressure on the mass flux of vapour q_v is of great interest.

If $K^* \gg D^*$ and $q_v z \ll K^* P_{atm}$ (this assumption depends on the order of magnitude of the thickness of the gaseous zone). This means that the mechanism is a pure diffusive one at constant pressure P_{atm}.

In this case, the mass flux of vapour q_v given by equation (8) equals q_{v0} defined as: the total pressure gradient vanishes in equation (5) and, the pressure equals the atmospheric one all over the medium

$$q_{v0} = -\frac{D^* \nabla P_v}{1 - \dfrac{P_v}{P_{atm}}}. \tag{9}$$

If $K^* \gg D^*$ only, we can suppose to a first approximation that the local pressure gradient ∇P_g is negligible without assuming that P_g is constant everywhere.

In the most general case, the value of the ratio, q_v/q_{v0}, is then:

$$\frac{q_v}{q_{v0}} = \frac{1 - \dfrac{P_v}{P_{atm}}}{\left(1 - \dfrac{P_v}{P_{atm}}\right) + \dfrac{P_v}{P_g}\dfrac{D^*}{K^*}} < 1. \tag{10}$$

$q_v/q_{v0} < 1$ is the consequence of the resistance to the barycentric movement of the gas through the vapour zone.

5.2. *Integration in the gaseous zone*

To analyse the spatial variations of pressure P_v in the thickness and to discuss the hypothesis made above, a model is developed based on the integration of the Darcy equation (6) for a fixed mass flux q_v given by equation (8).

The physical properties are assumed constant and calculated at a reference temperature of 100°C.

The integration of (6), from the interface $z = 0$ where $P_g = P_{atm}$ to the front located at z, gives:

$$P_g = -\frac{q_v}{K^*} z + P_{atm}. \tag{11}$$

By substituting in equation (8), it becomes:

$$\frac{D^*}{q_v} \nabla P_v + 1 + (D^* - K^*)\left(\frac{P_v}{P_{atm} K^* - q_v z}\right) = 0. \tag{12}$$

The analytic solution of the differential equation can be written as:

$$P_v = P_{atm}\left(-\frac{q_v}{P_{atm} K^*} z + 1\right) - P_{a\infty}\left(-\frac{q_v}{P_{atm} K^*} z + 1\right)^{(D^* - K^*)/D^*}. \tag{13}$$

5.3. *Influence of the permeability on the transfer modes*

The integration makes it possible to calculate the pressure of vapour needed to evacuate a given mass flux of vapour.

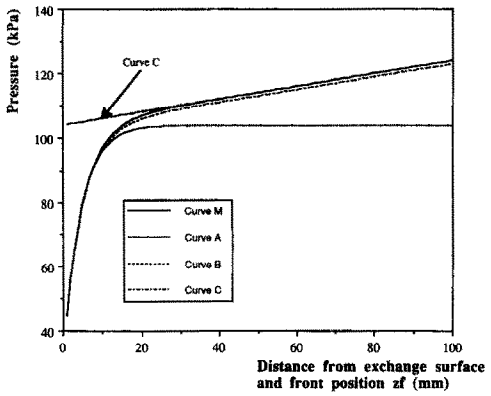

FIG. 23. Vapour pressure profiles between the exchange surface and the drying front. ($K = 10^{-13}$ m^2, $T_{wet} = 70$°C, $q_v = 1$ g m^{-2} s^{-1}.) Curve C represents the total gaseous pressure. These curves do not apply beyond the drying front.

The following figures (Figs. 23 and 24) show the variation of the vapour pressure with the position of the evaporation front for three values of the permeability: $K_g = 10^{-13}$ m^2 and 10^{-16} m^2 and a mass flux of vapour $q_v = 10^{-3}$ kg m^{-2} s^{-1}.

The wet bulb temperature is constant and equal to 70°C.

The analytic model, marked (M) and represented by a continuous line, is compared to:

- the pure diffusive model (marked (A)) for which $K^* \gg D^*$ and $q_v z \ll K^* P_{atm}$;
- the approximate model (marked (B)) for which $K^* \gg D^*$.

In this case, account is taken of the spatial variation on the total pressure through the thickness of the vapour zone, but the local total pressure is not considered in the expression for the diffusive flux.

- the variation of the total pressure according to Darcy's law (marked (C)).

Permeability $K_g = 10^{-13}$ m^2 (Fig. 23). At small front depths the curve (A) relating to a pure diffusive mode shows a steep increase. Then, as the vapour pressure draws nearer to the total pressure (straight line (C)), the pressure gradient decreases to finally become zero and reach a horizontal asymptote. This is a consequence of Fick's law, not taking into account the fluid viscosity.

With the help of the previous model, it can be seen that:

- close to the interface, i.e. for total pressures in the vicinity of the atmospheric pressure, the curve (M) resulting from the model is identical to the pure diffusive curve (A). In this region, the vapour pressure gradient is higher than the total pressure gradient;
- for larger front depths, the effect of the total pressure gradient on the vapour pressure becomes more marked. The vapour pressure therefore draws closer to the total pressure and finally reaches it.

At this moment, only pure vapour is present and the transfer mode is purely convective. It is interesting to note that the vapour pressure approaches the total pressure, due to the factor $(P_g \nabla P_v - P_v \nabla P_g)$ which tends towards zero (equation (5)).

Curve (B) indicates that the vapour pressure, given by the approximate model, is always below the total pressure.

Permeability $K_g = 10^{-16}$ m^2. In this case the general shapes of the curves are completely different (Fig. 24). Near the interface, the vapour pressure gradient is lower than the total pressure gradient. Then, when the front moves inside the material, the partial pressure of air increases and the transfer mechanism is not modified.

Permeability $K_g = 10^{-14}$ m^2. It is interesting to follow the changes in the curves for intermediate permeability, i.e. when the convection resistance increases from $K_g = 10^{-13}$ m^2 to $K_g = 10^{-16}$ m^2.

For $K_g = 10^{-14}$ m^2, the pure diffusive mechanism, represented by curve (A), is unchanged, but the superposition of curves (M) and (A) occurs for smaller thicknesses than in case $K_g = 10^{-13}$ m^2, owing to the very sharp increase of the total pressure. The decrease in permeability induces an increased resistance to the convective transport of vapour through the porous media. The vapour pressure reaches the total pressure for a larger front depth. A wider separation is also observed between curves (M) and (B).

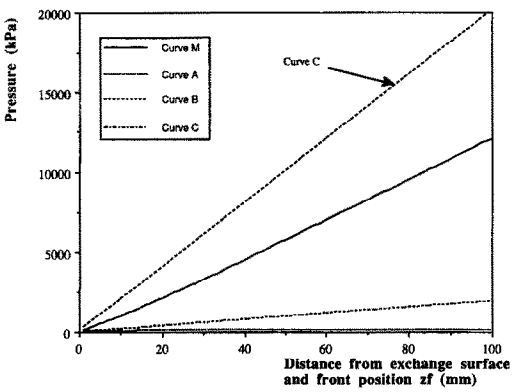

FIG. 24. Vapour pressure profiles between the exchange surface and the drying front. ($K = 10^{-16}$ m^2, $T_{wet} = 70$°C, $q_v = 1$ g m^{-2} s^{-1}.) Curve C represents the total gaseous pressure. These curves do not apply beyond the drying front.

5.4. *Dimensionless graphs*

The previous results can be presented in a dimensionless form, which involves drawing a synthetic graph. The dimensionless variables are as follows:

$$\begin{cases} Z^* = -\dfrac{q_v}{P_{atm} K^*} z & \left(\dfrac{\text{increase of total pressure}}{\text{atmospheric pressure}}\right) \\ B = \dfrac{K^*}{D^*} & \left(\dfrac{\text{diffusive resistance}}{\text{convective resistance}}\right). \end{cases}$$

Consequently the analytic model takes the form:

$$P_v = P_{atm}(Z^*+1) - P_{a\,r}(Z^*+1)^{1-B} \quad (14)$$

and the Darcy law can be written as:

$$P_g = P_{atm}(Z^*+1). \quad (15)$$

Figure 25 represents the variation of vapour pressure within the material as a function of the reduced depth Z^*, for different values of the coefficient B.

It can be seen that the pressure variations obey Darcy's linear law more rapidly when B is high. The main interest of the graph is to provide a set of curves enabling the phenomena to be studied for different values of the parameters.

5.5 *Comparison between experiments and theory*

For a given value of the mass flux of vapour q_v the analytical model enables calculation of the vapour pressure at the front (P_{vf}) vs its position z_f.

Since the high permeability of the porous media used (light concrete $K_g = 10^{-13}$ m^2) prevented pressure measurements, only temperature values can be considered.

Assuming local thermodynamic equilibrium at the front, it is possible to link the vapour pressure at the front P_{vf} to the temperature at the same point using the following relation:

$$P_{vs} = \exp\left(25.5058 - \frac{5204.9}{T_f+273}\right). \quad (16)$$

Therefore, for a given value of mass flux of vapour q_v, the analytical model expressed by equations (13) and (16) relates the front temperature T_f to its location z_f.

On the other hand, a simplified enthalpy balance (sensible heat requirements being neglected) gives a second relation between T_f and z_f.

This balance takes the form:

$$q_v \cdot \Delta h_v = (T_e - T_f)\cdot\left(\frac{z}{\lambda} + \frac{1}{h}\right)^{-1} \quad (17)$$

in which h and λ are experimentally evaluated in ref. [15].

For a given value of the mass flux of vapour q_v, the solution of the two equations ((13)-(16) and (17)) permits the determination of the two unknown variables: T_f and z_f.

Assuming the variation of the mass flux of vapour with time during drying to be known, the variation with time of $T_f(t)$ and $z_f(t)$ can be deduced and compared to the experimental results. The variation with time of q_v is obtained by derivation of the curve representing the weight loss of the slab vs time.

The curves $T_f(t)$ are plotted in Fig. 26 which shows the variation with time of the temperatures of five thermocouples: three located in the median plan of the slab and at different depths ($T5$ = 2 mm, $T4$ = 7.5 mm and $T3$ = 15 mm) and two located at 10 mm from the front ($T1$) and the rear ($T8$) ends of the slab.

Excellent overall agreement can be seen between the calculated and experimental temperatures of the front. In both cases a marked plateau at 86 C is first observed.

However, certain differences are observed with respect to the variations with time.

Thus, 220 min after the beginning of the drying process, a sharp increase in temperature is recorded on thermocouple ($T3$) at the centre of the slab, apparently indicating that at this moment the front depth is 15 mm from the surface, the whole material being in the hygroscopic range.

In contrast, the calculated temperature does not show the same variations as the experimental values. In effect, the analytical relation assumes the existence of a front whose position z_f tends towards infinity when the mass flux of vapour approaches zero.

From equations (14), (16) and (17) it can be demonstrated that the front temperature reaches a finite limit when the position z_f tends towards infinity. This limit explains the asymptote observed on the temperature calculated from the analytical model.

Assuming that the sharp temperature increase corresponds to the passage of the front, Table 1 has been drawn up comparing the experimental positions of the front to those calculated from the model based on the experimental mass flux of vapour.

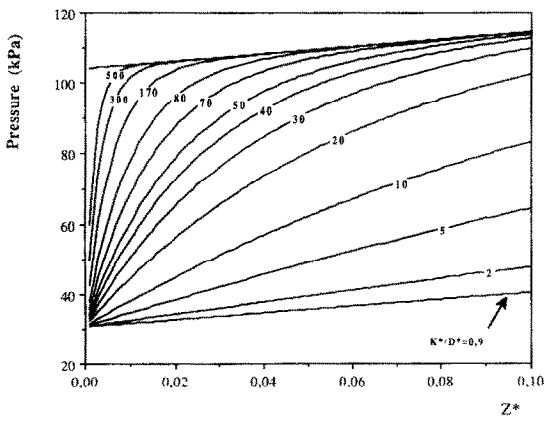

FIG. 25. Dimensionless graph of combined diffusive and convective vapour transport.

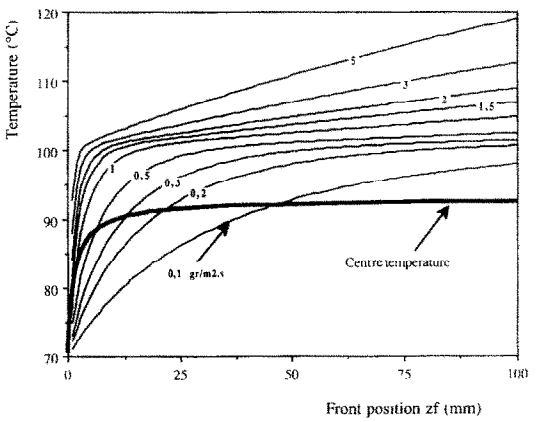

FIG. 26. Comparison between calculated and experimental temperatures.

Table 1.

Time (min)	Experimental front position (z_f)	Position given by the model (z_f)
95	2	11
160	7.5	23
220	15	43

It can be seen that the positions are very different. This is due to the distributions of moisture content within the slab during the drying process. As shown by the temperature–time curves, the ends of the slab ($T1$ and $T8$) dry faster than the middle part. This is the consequence of a higher heat transfer coefficient at the extremities, together with two-dimensional transfer at the periphery of the slab.

Thus, at the end of drying, only the central region of the slab is wet. By assuming the total mass flux of vapour to be distributed over the whole exchange surface, an overestimated local mass flux is therefore introduced into the analytical model.

Figure 27 shows the variations in temperature with front position, on which the results deduced from the enthalpy balance have been superimposed.

The figure clearly shows that the limiting temperature is due to the decrease of the mass flux of vapour when the front moves towards the centre of the slab.

6. CONCLUSION

High temperature convective drying has been analysed in three different ways, for two kinds of fluid (superheated steam and moist air) and two different materials (light concrete and softwood).

First, the experimental investigation used a wind tunnel and a new type of sensor which enables airtight measurements of both temperature and pressure at the same point within the medium.

Next, each experiment was simulated with the aid of a numerical model based on a very comprehensive formulation of heat and mass transfer in porous media. The model ran in 1-D for concrete and in 2-D for softwood, a strongly anisotropic medium.

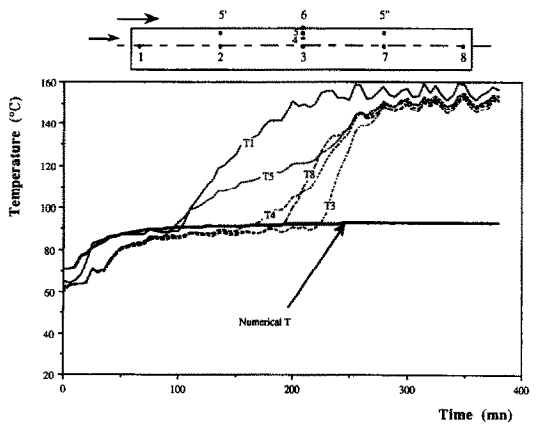

FIG. 27. Centre temperature vs front position. Note the decrease of drying rate as the front position increases.

Thirdly, a simplified analytic model, based on the concept of a drying front, points out how the vapour migration varies (diffusive, convective or both) vs the temperature and the properties of the medium.

As these three different approaches are in good agreement, very general conclusions can be drawn from this work. As a main result, we note that, generally, the process can be divided into three periods:

- an initial period, where the medium is at the wet bulb temperature;
- a second phase, with a stage more or less pronounced at a temperature which depends on the material. It is of course between the wet and the dry bulb temperatures;
- a final stage, during which all temperatures approach the dry bulb temperature.

Finally, an important point emerges from this study: the boiling point of water is rarely a temperature which results from an equilibrium between heat and mass transfers within the porous medium.

Indeed, for low permeable media, the temperature during the second period is greater than 100°C, while for media with a high vapour diffusivity, the latter is below 100°C (about 85°C for light concrete).

Nevertheless, large stages at the boiling point have often been observed in the literature.

Explanations for this do exist:

- for superheated steam, the wet bulb temperature equals the boiling point and the first drying period occurs at 100°C. Moreover, the temperature at the centre remains at this level during all the second drying period for media with high vapour diffusivity. In this case, the temperature which would result from the properties of the medium is actually hidden by a too high value of the wet bulb temperature;
- when the permeability of the medium is low and when there is a leak from the sensor, there will be local boiling and an artificial stage at the boiling point appears during the second drying period. This phenomenon occurs for both superheated steam and moist air.

REFERENCES

1. C. Basilico, Le séchage convectif à haute température du bois massif, Thèse d'État, LEMTA-INPL/CNRS Nancy (1985).
2. C. Basilico and M. Martin, Approche expérimentale des mécanismes de transfert au cours du séchage convectif à haute température d'un bois résineux, *Int. J. Heat Mass Transfer* **27**, 657–668 (1984).
3. M. Moser, P. Perre and M. Martin, Remise en cause du palier à 100°C lors du séchage convectif de résineux en vapeur surchauffée, Colloque SFT 90, Vol. 2, pp. 239–243, Nantes (1990).
4. R. Northway, Moisture profiles and wood temperature during very high temperature drying of pinus radiata explain lack of degrade, *Upgrading Wood Quality Through Drying Technology, IUFRO 1989 Wood Drying*

Symposium, pp. 24–28, Seattle, Washington (1989).
5. J. N. Beard, H. N. Rosen and B. A. Adesanya, Temperature distribution in lumber during impingement drying, *Wood Sci. Tech.* **19**, 277–286 (1985).
6. F. Kayihan, Moisture movement, *Upgrading Wood Quality Through Drying Technology, IUFRO 1989 Wood Drying Symposium*, pp. 255–268, Seattle, Washington (1989).
7. M. A. Stanish, G. S. Schajer and F. Kayihan, A mathematical model of drying for hygroscopic porous media, *A.I.Ch.E. Jl* **32**(8), 1301–1311 (1986).
8. P. Perre, Le séchage convectif de bois résineux: choix, validation et utilisation d'un modèle, Thèse de Doctorat, Paris VII (1987).
9. P. Perre and D. Maillet, Drying of softwood: the interest of a two dimensional model to simulate anisotropy or to predict degrade 3, *Upgrading Wood Quality Through Drying Technology, IUFRO 1989 Wood Drying Symposium*, pp. 131–137, Seattle, Washington (1989).
10. P. Perre and A. Degiovanni, Simulation par volumes finis des transferts couplés en milieux poreux: séchage du bois à basse et à haute température, *Int. J. Heat Mass Transfer* **33**, 2463–2478 (1990).
11. S. Whitaker, Simultaneous heat, mass and momentum transfer in porous media: a theory of drying, *Advances in Heat Transfer*, Vol. 13, pp. 119–203. Academic Press, New York (1977).
12. S. V. Patankar, *Numerical Heat Transfer and Fluid Flow*. Hemisphere, New York (1980).
13. S. Ben Nasrallah and P. Perre, Detailed study of a model of heat and mass transfer during convective drying of porous media, *Int. J. Heat Mass Transfer* **31**, 957–967 (1988).
14. P. Perre and C. Moyne, Processes related to drying: Part II—Use of the same model to solve transfers both in saturated and unsaturated porous media, *Drying Tech.* **9**(5), 1153–1179 (1991).
15. A. Azizi, C. Moyne and A. Degiovanni, Approche expérimentale et théorique de la conductivité thermique des milieux poreux humides—I. Expérimentation, *Int. J. Heat Mass Transfer* **31**, 2305–2317 (1988).
16. O. Krischer and K. Kroll, Technique du séchage, Tomes 1,2,3, C.E.T.I.A.T., Orsay (Traduit du texte original de 1963).
17. F. O. Teroso, O. K. Kimbler and E. T. Choong, Determination of the relative permeability of wood to oil and water, *Wood Sci.* **5**(1), 21–26 (1972).

APPENDIX 1: FORMULATION AND BOUNDARY CONDITIONS

The set of equations governing heat, mass and momentum transfers in granular or hygroscopic porous media has been derived elsewhere [10, 11, 13]. Details of the developments and assumptions are available in these papers. The aim of this appendix is to describe precisely the physics simulated by the numerical code.

All the quantities used in the equations are averaged over the REV (Representative Elementary Volume, $\mathscr{V}$). The averaged quantities are defined as:

$$\bar{\psi} = \frac{1}{\mathscr{V}} \int_{\mathscr{V}} \psi \, \mathrm{d}\mathscr{V} \quad \text{for the spatial average} \tag{A1}$$

and

$$\bar{\psi}^{\alpha} = \frac{1}{\mathscr{V}_{\alpha}} \int_{\mathscr{V}_{\alpha}} \psi \, \mathrm{d}\mathscr{V} \quad \text{for the intrinsic phase average.} \tag{A2}$$

The porous medium is made up of three or four phases (s = solid, l = liquid, g = gaseous and, eventually, b = bound water). In the following equations, a bold letter denotes a vector and a sign $\approx$ denotes an order 2 tensor. The apparent density of the porous media ρ_0 is defined by:

$$\rho_0 = \bar{\rho}_s. \tag{A3}$$

Mass conservation equations:

liquid phase

$$\rho_l \frac{\partial \varepsilon_l}{\partial t} + \nabla \cdot (\rho_l \bar{\mathbf{u}}_l) = -\langle \dot{m} \rangle \tag{A4}$$

gaseous phase

$$\frac{\partial \bar{\rho}_g}{\partial t} + \nabla \cdot (\bar{\rho}_g^g \bar{\mathbf{u}}_g) = \langle \dot{m} \rangle + \langle \dot{m}_b \rangle \tag{A5}$$

vapour only

$$\frac{\partial \bar{\rho}_v}{\partial t} + \nabla \cdot (\bar{\rho}_v^g \bar{\mathbf{u}}_v) = \langle \dot{m} \rangle + \langle \dot{m}_b \rangle \tag{A6}$$

bound water (case of wood)

$$\frac{\partial \bar{\rho}_b}{\partial t} + \nabla \cdot (\overline{\rho_b \mathbf{u}_b}) = -\langle \dot{m}_b \rangle. \tag{A7}$$

Transport equations:

Generalized Darcy's law

$$\bar{\mathbf{u}}_g = -\frac{\bar{\bar{K}}_g \cdot \bar{\bar{k}}_g}{\mu_g} \nabla (\bar{P}_g^g) \tag{A8}$$

$$\bar{\mathbf{u}}_l = -\frac{\bar{\bar{K}}_l \cdot \bar{\bar{k}}_l}{\mu_l} \nabla (\bar{P}_l^l) \tag{A9}$$

with

$$\bar{P}_l^l = \bar{P}_g^g - P_c \tag{A10}$$

bound water diffusion

$$\overline{\rho_b \mathbf{u}_b} = -\bar{\rho}_c \bar{\bar{D}}_b \nabla \left(\frac{\bar{\rho}_b}{\bar{\rho}_c} \right) \tag{A11}$$

gaseous diffusion

$$\bar{\rho}_v^g \bar{\mathbf{u}}_v = \bar{\rho}_v^g \bar{\mathbf{u}}_g - \bar{\rho}_v^g \bar{\bar{D}}_{\mathrm{eff}} \nabla \left(\frac{\bar{\rho}_v}{\bar{\rho}_g} \right). \tag{A12}$$

Energy conservation:

The enthalpy balance

$$\frac{\partial}{\partial t} (\overline{\rho h}) + \nabla \cdot (\overline{\rho \mathbf{u} h}) = \nabla \cdot (\bar{\bar{\lambda}}_{\mathrm{eff}} \nabla \bar{T}) \tag{A13}$$

gives the equation governing the temperature:

$$\overline{\rho C_p} \frac{\partial \bar{T}}{\partial t} + \Delta h_v (\langle \dot{m} \rangle + \langle \dot{m}_b \rangle) + h_v \langle \dot{m}_b \rangle - \overline{\rho_b \mathbf{u}_b} \nabla (h_v) + \left[(\rho_l \bar{\mathbf{u}}_l + \overline{\rho_b \mathbf{u}_b}) C_{pl} + \sum_{i=a,v} (\bar{\rho}_i^g \bar{\mathbf{u}}_i C_{pi}) \right] \cdot \nabla \bar{T} = \nabla \cdot (\bar{\bar{\lambda}}_{\mathrm{eff}} \nabla \bar{T}). \tag{A14}$$

Boundary conditions:

On a plane of symmetry, the fluxes of energy, moisture and dry air, equal zero:

$$[\bar{\bar{\lambda}}_{\mathrm{eff}} \nabla \bar{T} + \overline{\rho_b \mathbf{u}_b} h_v + (\rho_l \bar{\mathbf{u}}_l + \overline{\rho_b \mathbf{u}_b}) \Delta h_v] \cdot \mathbf{n} = 0$$

$$[\rho_l \bar{\mathbf{u}}_l + \bar{\rho}_v^g \bar{\mathbf{u}}_v + \overline{\rho_b \mathbf{u}_b}] \cdot \mathbf{n} = 0$$

$$\bar{\mathbf{u}}_a \cdot \mathbf{n} = 0. \tag{A15}$$

On a convective surface, the total pressure of the gaseous phase equals the atmospheric pressure and heat and mass transfer come from exchange coefficients:

$$\bar{P}_g^g = P_{\mathrm{atm}}$$

$$[\bar{\bar{\lambda}}_{\mathrm{eff}} \nabla \bar{T} + \rho_l \bar{\mathbf{u}}_l h_v + (\rho_l \bar{\mathbf{u}}_l + \overline{\rho_b \mathbf{u}_b}) \Delta h_v] \cdot \mathbf{n} = h (\bar{T}_0 - T_s)$$

$$[\rho_l \bar{\mathbf{u}}_l + \bar{\rho}_v^g \bar{\mathbf{u}}_v + \overline{\rho_b \mathbf{u}_b}] \cdot \mathbf{n} = k c M_v \frac{2.2}{2.2 - x_{v0} - x_{v,s}} (x_{v0} - x_{v,s}). \tag{A16}$$

A corrective factor appears in the expression of mass flux.

This term, which comes from the film theory, tends to infinity in the case of pure vapour: at this moment, the resistance to external moisture transfer equals zero. In the simulation, the corrective factor has been limited to 11. This is enough to obtain with great accuracy the real boundary condition that undergoes in this case:

$$\bar{P}_v^g = P_{atm}. \quad \text{(A17)}$$

APPENDIX 2: PHYSICAL CHARACTERISTICS USED IN THE SIMULATION

The set of equations described in Appendix 1, the perfect gases law and the assumption of local thermodynamic equilibrium leads to a description of the porous medium by three state variables and three coupled and non-linear differential equations. The numerical method is described in other papers [8, 10, 13]. The physical characteristics used in the simulations are listed below:

T is the local temperature (°C): $T = \bar{T}$ (T_k is the temperature in K);

X is the moisture content: $X = \dfrac{\varepsilon_l \rho_l + \bar{\rho}_v + \bar{\rho}_b}{\rho_0}$;

P is the pressure of the gaseous phase (Pa): $P = \bar{P}_g^g$.

1. *Light concrete*

Remark: for this medium, use is made of results concerning liquid migration for steady state experiments [16]. The liquid migration coefficient, named a_{ml}, defined in this way is connected to the capillary pressure by the following equation:

$$\rho_0 \cdot \tilde{a}_{ml} = \rho_l \frac{\tilde{\bar{K}}_l \cdot \tilde{k}_l}{\mu_l} \frac{\partial p_c}{\partial X}.$$

Porosity: $\Pi = 0.80$.
Density of the solid matrix: $\rho_0 = 500$ (kg m^{-3}).
Instrinsic permeability: $K = 10^{-13}$ (m^{-2}).
Irreducible moisture content: $X_{irr} = 0.30$.
Heat capacity: $\overline{\rho C_p} = \rho_0(840 + 4185X)$ (J kg^{-1} °C^{-1}).
Vapour pressure:

$$P_v = P_{vs} \quad \text{when } X \geqslant 0.07$$

$$\frac{P_v}{P_{vs}} = \frac{X}{0.07} \times \left[2 - \frac{X}{0.07}\right] \quad \text{when } X \leqslant 0.07.$$

Relative permeabilities:

$$k_{rl} = X^{*3} \quad \text{with } X^* = \frac{X - X_{irr}}{X_{sat} - X_{irr}}$$

$$k_{rg} = 1 + (2X^* - 3)X^{*2}.$$

Liquid migration coefficient: $\log_{10}(\rho_0 \cdot a_{ml}) = \sum_{i=0}^{5} a_i X^i$

$$a_0 = -10.5; \quad a_1 = 30.54; \quad a_2 = -70.75; \quad a_3 = 83.97;$$
$$a_4 = -49.92; \quad a_5 = 11.88.$$

Gaseous diffusion: $D_{eff} = 0.2 \times D_v$
(D_v is the mass diffusivity of vapour in air).
Thermal conductivity: $\lambda = 0.142 + 0.46X$ (W m^{-1} °C^{-1}).

2. *Softwood*

All the experiments have been carried out with a light softwood (Abies grandis). Its density is lower than Spruce: the permeabilities chosen here are higher than those used in the previous paper [10]. Moreover, some problems on relative permeabilities were pointed out in the same paper. Consequently, the relative permeability curves are quite different too (Fig. A1):

In the transverse direction, they have to be lower in the domain of low moisture content.

In the longitudinal direction, most of the liquid flux comes from the effect of gaseous pressure rather than from the capillary action. This is very close to the experiments of relative permeabilities carried out by Teroso *et al.* [17]. The new curves have been chosen in order to fit the experimental results available in the domain of high moisture content.

Porosity: $\Pi = 0.733$.
Density of the solid matrix: $\rho_0 = 400$ (kg m^{-3}).
Heat capacity:

$$\overline{\rho C_p} = \rho_0(1113 + 4.85T + 4185X) \text{ (J kg}^{-1}\text{ °C}^{-1}\text{)}.$$

Vapour pressure:

$$P_v = P_{vs} \exp\left[(-3.3527 - 0.01328T + 23.63 \times 10^{-5} T^2) \times (0.8487 - 67.4 \times 10^{-5} T)^{92X}\right].$$

Bound and free water: $X = X_b + X_l$
where $X_b = \min(X_{lsp}, X)$ and $X_{lsp} = 0.325 - 0.001T$ (at full saturation, $X_{sat} = X_{lsp} + X_{lsat}$).
Capillary pressure: $P_c = 1.364 \times 10^5 \sigma(X_l + 1.2 \times 10^{-4})$.

Transverse direction (T):
Intrinsic permeability:
- for liquid: $K = 5 \times 10^{-16}$ (m^2);
- for gas (with pits aspiration): $K = 10^{-16}$ (m^2).

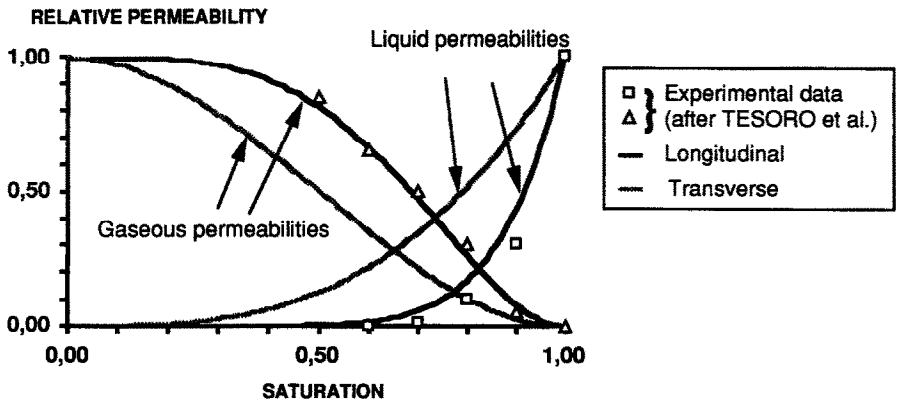

FIG. A1. Relative permeability curves used for softwood in the simulation.

Relative permeabilities: $k_{rl} = X^{*3}$ with $X^* = \dfrac{X_l}{X_{lsat}}$

$$k_{rg} = 1+(2X^*-3)X^{*2}.$$

Gaseous diffusion: $D_{eff} = 10^{-3} \times D_v$
(D_v is the mass diffusivity of vapour in air).
Thermal conductivity (W m^{-1} °C^{-1}):

$X \geqslant 0.4$, $\lambda_{eff} = (0.65/100X+0.0932)$

$$\times (1+3.65\times 10^{-3}T)(0.986+2.695X)$$

$X \leqslant 0.4$, $\lambda_{eff} = (0.129-0.049X)(1+(2.05+4X)\times 10^{-3}T)$

$$\times (0.986+2.695X).$$

Bound water diffusion:

$$D_b = \exp\left[-9.9+9.8X-\frac{4300}{T_k}\right] (T_k \text{ in Kelvin}).$$

Longitudinal direction (L):
Intrinsic permeability:
- for liquid: $K = 5\times 10^{-13}$ (m^2);
- for gas (with pits aspiration): $K = 10^{-13}$ (m^2).

Relative permeabilities: $k_{rl} = X^{*8}$ with $X^* = \dfrac{X_l}{X_{lsat}}$

$$k_{rg} = 1+(4X^*-5)X^{*4}.$$

Gaseous diffusion: $D_{eff}(L) = 20 \times D_{eff}(T)$
(D_v is the mass diffusivity of vapour in air).
Thermal conductivity (W m^{-1} °C^{-1}): $\lambda_{eff}(L) = 2 \times \lambda_{eff}(T)$.
Bound water diffusion: $D_b(L) = D_b(T)$.

APPENDIX 3: SUMMARY OF ALL TESTS AND RUNS

Experimental tests

Medium	Test	Dry-bulb (°C)	Wet-bulb (°C)	Air flow (m s^{-1})	X_{in} (%)
Light concrete	1	140	≈100	6	90
	2	115	85	4	100
	3	160	70	10	108
Softwood	4	160	≈100	10	165
	5	115	82	5	180
	6	140	82	7	140

Numerical runs

Medium	Run	Dry-bulb (°C)	Wet-bulb (°C)	Heat transfer (W m^{-2} °C^{-1})	X_{in} (%)
Light concrete	1	140	98	30	90
	2	115	85	25	100
	3	160	70	35	110
Softwood	4	160	98	30	170
	5	115	82	20	180
	6	140	82	25	140

Remark: With the aid of an enthalpy balance, the heat transfer coefficient is deduced from the maximal drying rate obtained during the experiment. For a similar velocity, the latter is a little smaller for softwood than for aerated concrete. In fact, the slabs of concrete (0.6 m long) are smaller than the boards (1 m long): the decrease of the transfer coefficient along the air flux causes the average exchange to be smaller for longer geometries.